



Tunable optical properties of Fe₂O₃ magnetic nanoparticles synthesized from Ferritin

Sunil Kumar¹ · Manoj Kumar¹ · Srihari Velaga² · Amarjeet Singh¹

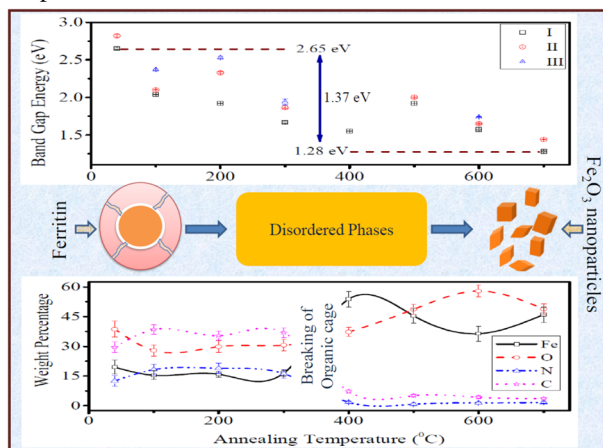
Received: 19 April 2022 / Accepted: 6 November 2022 / Published online: 16 December 2022
© The Author(s), under exclusive licence to Springer Science+Business Media, LLC, part of Springer Nature 2022

Abstract

The optical properties of a precursor dry Ferritin powder and its iron oxide derivatives were studied using UV–visible spectroscopy. The iron oxide derivatives were synthesized by applying controlled heat treatment up to 700 °C. The optical properties show dramatic variation in absorption spectra through a large shift in absorption band edge as a function of annealing temperature. On one side (40 °C) we have precursor Ferritin powder and on the other side (700 °C) a crystalline hematite phase along with disordered phases at intermediate temperatures. Energy dispersive x-ray (EDX) analysis and XRD reveal that crystallization and thermal destruction of organic cage are inter-related. As ferrihydrite complexes inside the Ferritin cavity go through solidification from amorphous Fe₂O₃ to hematite crystalline phase (α -Fe₂O₃), the heterogeneity of electronic excitation processes occurs through ligand-to-metal charge transfer (LMCT), pair excitation and ligand field (d-d) transition. Strong magnetic induction in the intermediate range (400–500 °C) was associated with the enhancement of the pair excitation process. As the material changes phases due to annealing, a large absorption band edge shift from 2.65 to 1.28 eV, a total red shift of 1.37 eV, provides a simple approach to tuneable optical properties of iron oxides.

Graphical abstract

Top panel shows the variation of optical band gap, whereas bottom panel describe the weight percentage variation of different elements with annealing temperature. Middle panel presents the entire theme in form of a sketch of the process related to the synthesis of different phases.



✉ Amarjeet Singh
amarjeet.sirohi@gmail.com

¹ Department of Physics, Himachal Pradesh University,

Shimla 171005, India

² High Pressure and Synchrotron Radiation Physics Division,
Bhabha Atomic Research Centre, Mumbai 400085, India

Keywords Nanoparticles · Ferritin · Transition metal oxides · Magnetic ordering · Optical band gap · d-d transition

Highlights

- Ferritin, a biomacromolecule, was used to synthesize nanomaterials with variable optical properties in a sol–gel technique.
- The variation originates from the structure of nanomaterials which include disordered and crystalline phase of Fe_2O_3 as a function of annealing temperature.
- The presence of a large tunable range (1.37 eV) of band gap that covers the entire visible range from blue to red end of the spectrum.
- EDX and XRD measurements show correlation between thermal destruction of the organic core and crystallization of hematite phase.
- The pair-excitation transition becomes stronger than LMCT in mid temperature range (400–500 °C) as result of strong magnetic coupling.

1 Introduction

Transition metal oxides (TMOs) are fascinating materials for their rich optical and magnetic properties [1–3]. The bulk phase of hematite ($\alpha\text{-Fe}_2\text{O}_3$) shows very weak magnetic induction due to the anti-ferromagnetic coupling of two interpenetrating sub-lattices [4, 5]. In principle, the net magnetization would be zero due to the mutual cancellation of spins of two sub-lattices but the presence of spin canting results in non-zero net magnetization that is often very weak. However when crystalline particles are of few tens of nanometers or less, surface disorder results in strong magnetization since the exact cancellation of spins is offset by lattice disorder. In our recent study, we had shown that the small size nanocrystalline $\alpha\text{-Fe}_2\text{O}_3$ nanoparticles show stronger magnetization as compared to larger particles [6]. The $\alpha\text{-Fe}_2\text{O}_3$ nanoparticles find applications in photocatalysis, water splitting, hyperthermia treatment, ferrofluids, memory devices and spintronics [7–11]. The studies of TMOs in general and $\alpha\text{-Fe}_2\text{O}_3$, in particular, had been carried out widely from a different perspective using chemical synthesis routes [1, 12, 13]. In recent times, biomimetic synthesis has become popular due to gaining control over particle size and shape [6, 14–16]. Ferritin is a biomacromolecule that houses around 2000 Fe ion complexes inside a soft shell of polypeptides. It gives a way for a template synthesis of mono-disperse nanoparticles [14]. Biomimetic synthesis achieved much success yet the idea is far from being fully exploited. In general, bio macromolecules find mention in materials science as biomaterials for advanced applications [14–23]. We need to devise ways and strategies for better control of particle size and shape for obtaining predictable properties and applications. It requires a lot of ground work with a view of different aspects of synthesis and their physical properties. In this article, we discuss the optical properties of the various phases of Fe_2O_3 synthesized from Ferritin using sol–gel method [12, 24]. In

a two-step process, a liquid colloidal suspension of Ferritin was dried on the solid surface at a slightly elevated temperature of 40 °C. In the next “firing” stage, the samples were heat treated at different temperatures from 100–700 °C with a gap of 100 °C for each successive sample. The temperature range was sufficient to destroy the organic shell and to promote calcinations and crystalline growth in the samples. The iron compound in the cavity goes through ferrihydrite to amorphous Fe_2O_3 , and then finally it changes to hematite crystalline phase in the same temperature range of annealing [6]. The purpose of the present experimental work was to study optical properties as the system passes through different structural phases. Scanning electron microscopy (SEM) and x-ray diffraction (XRD) were used to analyze the nanoscale morphology and atomic structure of the specimen. Energy dispersive x-ray (EDX) was used for finding the relative concentration of elements. A vibrating sample magnetometer (VSM) was used to study magnetic properties. UV–VIS spectroscopy was used to study optical absorption properties for analysis of spectral distribution and band structure. Grazing incidence XRD at synchrotron source (INDUS-II) was used to analyze crystal structure and distribution of orientations.

In a way, this study is unique. The set of samples comprises dried Ferritin shells loaded with ferrihydrite molecules on one side (40 °C) and crystalline $\alpha\text{-Fe}_2\text{O}_3$ phase on another side (700 °C). At all other intermediate temperatures, several phases of material exist including amorphous and crystalline nanoparticles. Various studies of optical properties of Fe_2O_3 are reported in the published literature of experimental and theoretical work [25–27]. But the shift in the band edge as high as 1.37 eV was not found in any of the earlier reported work. The band gap tuning of $\alpha\text{-Fe}_2\text{O}_3$ due to sulfur doping was reported to change the band gap to around 0.75 eV [28]. In our case, it is the activation of different processes such as pair-excitation, ligand field transition beyond LMCT that contribute to absorption in

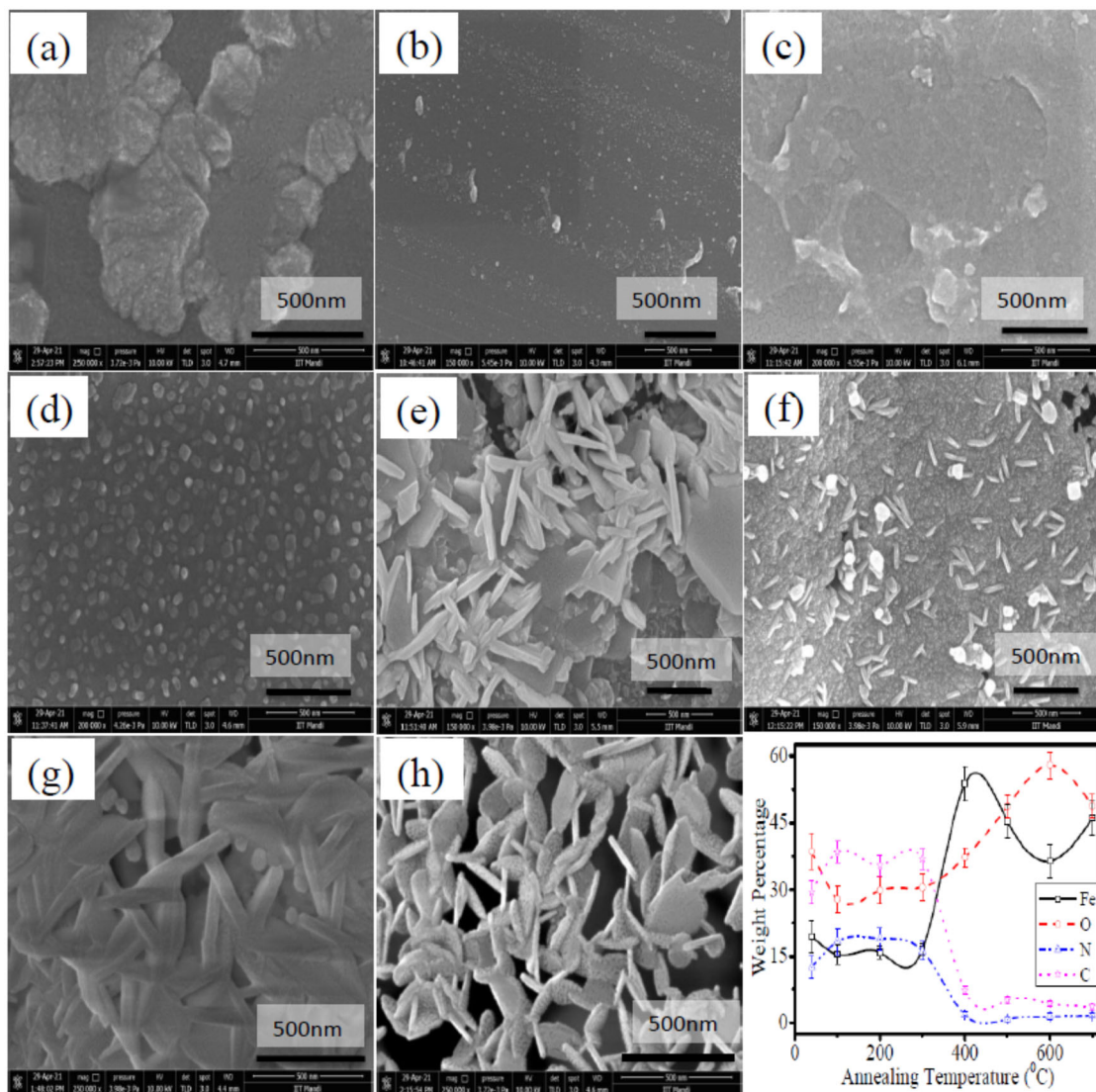


Fig. 1 The SEM micrograph obtained at 10 kV (JFEI Nova Nano SEM-450) for the samples 40 °C (as prepared) (a), and annealing at 100 (b), 200 (c), 300 (d), 400 (e), 500 (f), 600 (g) and 700 °C (h). The

different range. Fe is a transition element that is responsible for strong magnetic and rich optical spectra in the visible region due to d-d transitions. The environment of Fe ion changes from being local to non-local for electronic transition and spin correlation, it forms a rich system in terms of magnetic and optical properties [1].

2 Materials and methods

Aqueous suspension of Ferritin was purchased from Sigma-Aldrich and it was stored at a low temperature (<8 °C) in a refrigerator. A set of eight samples was prepared using the sol-gel method for UV-VIS measurements. In the first step, a measured volume of suspension was poured on clean Si (100) substrates equilibrated at

bottom-right corner shows the weight percentage of different elements found using EDX in all samples treated at different temperatures

40 °C on a hot plate for 20 min. In the second step, the seven samples were sintered for 1 h at seven different temperatures from 100 to 700 °C with a gap of 100 °C for each next sample using a muffle furnace (Khera, model no. KI-179 B) with a deviation of ± 4 °C. One of the samples was kept “as prepared” (40 °C) for reference. Afterward, the dry powder was removed from substrates using a spatula. Then powder was suspended in glycerol and the suspension was homogenized using an ultrasonic bath (KUDOS, Model SK2210HP). The suspension was quite stable for days. The concentration of the solution for measurement is 0.25 mg/ml. The UV 3000⁺ spectrometer (LABINDIA, Model: UV 3000⁺ UV/VIS Spectrophotometer) was used to acquire the data with subtracted background. The scanning range of the wavelength was from 190 to 800 nm with a step size of 2 nm.

The same powder sample was also used for the magnetic measurements using a VSM (Lake Shore VSM, Model: 7410 Series VSM) which is facilitated with a dynamic range from 1×10^{-7} to 10^3 emu with an accuracy of $\pm 0.5\%$ plus noise which is $0.75 \mu\text{emu}$ at maximum. The samples were loaded in the vibrating rod sample holder, and then they were placed between the magnetic coils. The magnetic field was swept from -20 to $+20$ kilo Oersted (kOe) and a complete cycle of magnetic induction measurement took around 40 min for each sample at room temperature. The low temperature (15–305 K) magnetic study was performed to obtain the zero-field cooled (ZFC) and field cooled (FC) curves. The samples for microscopy study and XRD were prepared using the identical method on Si (100) substrates. But there was no need to peel off the powder from the substrate. Measurements were performed on dried films on the substrate directly. The SEM operated at 10 kV (JFEI Nova Nano SEM-450) was used to study the surface morphology of the samples. EDX spectroscopy was carried out on the same sample for estimating elemental composition in a single lot without breaking a vacuum. Two-dimensional (2D) XRD was carried out in grazing incidence geometry at photon energy of 10 keV at BL-11 beamline of INDUS-II synchrotron at Raja Ramanna Center for Advanced Technologies in India. In grazing incidence geometry (GID-2D), 2D intensity maps were recorded to analyze any preferential orientation of crystallites to the substrate on the MAR3450 image plate detector. Data acquisition time was 30 min for each measurement. The wave vector q define as; $q = 2\pi (\sin \alpha + \sin \beta) / \lambda$. The grazing angle of incidence (α) was kept fixed at 0.5° .

3 Analysis of results

3.1 Scanning electron microscopy

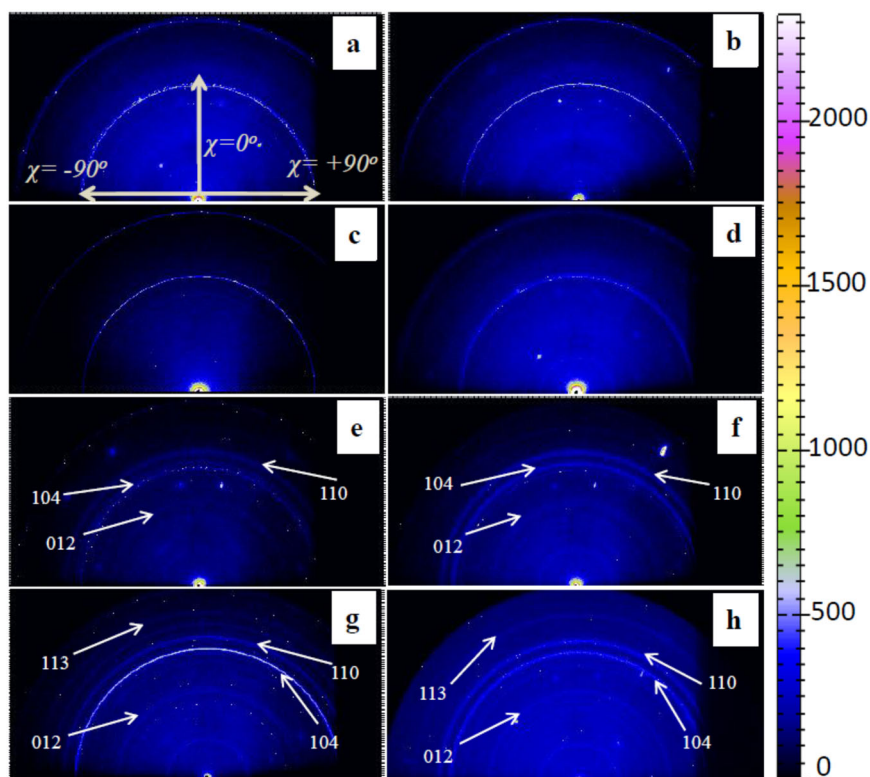
The surface morphology of the samples was studied using a scanning electron microscope. Figure 1 shows the micrographs corresponding to samples treated at all different temperatures from panel (a) to (h). The morphology of the “as prepared” sample (a) appears as aggregated mass or clumps of materials or Ferritin. The surface morphology in panels (b, 100°C) and (c, 200°C) appears quite homogeneous. Some granular structure is noted in panels (d, 300°C), whereas panels (e, 400°C), (f, 500°C) and (g, 600°C) show needle-shaped objects. The panel (h, 700°C) illustrates flake-like objects. These flakes, when looked at carefully, have their own granular internal structure. From these observations, it became quite obvious that estimation of particle size and shape from the surface morphology is difficult. One main reason is that the inorganic iron oxide phase is buried deep inside the organic shells. A lump of such material often appears continuous

medium. Even after the thermal decomposition of the organic shell, the debris of the organic shell remains mixed with the iron oxide particles. Particle size often becomes clearly visible under SEM when low concentration sol gets dried on the surface with clear separation among particles. In all microscopy techniques, it is often a challenge to locate such a tiny portion of the area on a macroscopically large sample surface. The surface morphology, though, has no relation to magnetic and optical properties since these specimens were peeled off the substrate before making magnetic and optical measurements. It is mainly the phase change of iron oxide particles that affects the physical properties. The determination of particle size using XRD and SEM has been achieved earlier [6]. EDX measurements were also performed on the samples for determining the weight percentage ratio of the elements in the bottom-right corner of Fig. 1.

Iron (Fe) is mainly present in the core of the Ferritin molecule, whereas carbon (C) and nitrogen (N) forms the organic shell. Oxygen (O) is usually present in the core as well as in the organic shell. In the temperature range from 300 – 400°C , the relative concentration of carbon and nitrogen significantly drops, whereas iron and oxygen concentration relatively goes up. This prominent change in relative elemental concentrations marks the phenomenon of “burning down” of the organic shell as it cannot withstand such high temperature. It appears that a portion of carbon and nitrogen elements smokes out as gases on the burning of organic shell. After 400°C , the sample consists of a relatively larger concentration of iron and oxygen elements. The increase in Fe and O weight percentage represents the relative increase because of the absence of other elements at a higher temperature. XRD study of the samples was published earlier which relate temperature dependent evolution of structural phases with magnetic properties [6]. It was found that there was no signature of crystallization of Fe_2O_3 up to 400°C , a feeble signature of $\alpha\text{-Fe}_2\text{O}_3$ were seen at 500°C , which were unambiguously confirmed at 700°C . The crystallite size determined using Scherrer formula, grew from ~ 23 to ~ 50 nm. Below 400°C , since there was no peak corresponding to Fe_2O_3 , It is obvious that particles were amorphous. Machala et al. coined the term “x-ray amorphous” for particles smaller than 5 nm [29]. However, DSC indicates amorphous to crystalline phase transition close to 500°C [6]. The amorphous phase lying in intermediate temperature range (400 – 500°C) is characterized with stronger magnetization as compared to crystalline phase (700°C) and molecular phase (40°C). It is interesting to relate EDX finding with XRD results: the temperature assisted destruction of organic shell takes place at 400°C , while the crystallization took place at 500°C and above, revealing the important mechanism of crystallization and particle growth.

As the phase identification of Fe_2O_3 and its structural evolution was already known, we carried out 2D diffraction

Fig. 2 Two-dimensional intensity maps of the samples obtained using GIXRD technique at a fixed angle of incidence of 0.5° . The different panels represent different annealing temperatures: **a** 40°C (as prepared), **b** 100°C , **c** 200°C , **d** 300°C , **e** 400°C , **f** 500°C , **g** 600°C and **h** 700°C



study to analyze the orientation distribution of crystallites. The 2D diffraction patterns from all samples are shown in Fig. 2. In the case of preferred orientation, the intensity from a given crystalline plane would be converging to a spot in a certain direction [30]. The observed semi-circular rings with uniform intensity throughout are a clear signature of the random distribution of crystalline planes. In the diffraction terminology, we say that there is a powder nature of the crystallites observed. We begin with the identification of the sample annealed at 700°C where the nucleated crystallites are grown to a large extent for unambiguous identification of phase. The hematite phase ($\alpha\text{-Fe}_2\text{O}_3$) was confirmed with the four characteristic rings indexed as (012), (104), (110) and (113) as seen in Fig. 2h (listed in Table 1). In the middle range of annealing $400\text{--}500^\circ\text{C}$, only (104) and (110) planes generate prominent intensity, whereas (012) plane generate feeble intensity and (113) was absent. At the lower temperature range ($40\text{--}400^\circ\text{C}$), the $\alpha\text{-Fe}_2\text{O}_3$ phase could not be identified as the diffraction ring at $q = 2.235$ remains unidentified which is likely to be originated from the organic matrix or some planes of FeOOH [6]. This uncharacteristic diffraction ring was not seen for heat treatment at 400°C and above. We had similar kinds of observations in our earlier studies on a similar set of samples using high-resolution conventional XRD [6]. Figure 3 shows the diffraction profiles of all samples obtained from each 2D intensity map (panel) in Fig. 2 by integrating intensity along polar angle (χ) from -90° to $+90^\circ$ along with the semi-circular rings. This way it

Table 1 Comparison of observed XRD peaks of the samples with standard peaks given in JCPDS card (87-1164) of $\alpha\text{-Fe}_2\text{O}_3$ phase

Ann.temp ($^\circ\text{C}$)	$\alpha\text{-Fe}_2\text{O}_3$ phase (hkl)	$q(\text{nm}^{-1})$ JCPDS data ($\alpha\text{-Fe}_2\text{O}_3$)	$q(\text{nm}^{-1})$ (Observed)
400	(012)	1.71	1.715
	(104)	2.33	2.354
	(110)	2.50	2.510
500	(012)	1.71	1.716
	(104)	2.33	2.358
	(110)	2.50	2.507
600	(012)	1.71	1.720
	(104)	2.33	2.332
	(110)	2.50	2.512
	(113)	2.85	2.857
700	(012)	1.71	1.713
	(104)	2.33	2.335
	(110)	2.50	2.504
	(113)	2.85	2.857

appears as a conventional (1-dimensional) XRD plot with lower resolution as collimating slits are not used in 2D grazing incidence diffraction. The intensity peaks do not appear sharp as often seen in the conventional XRD pattern. Therefore, any kind of peak shape analysis would provide a dubious interpretation here. The peak shape analysis had been done earlier using high-resolution conventional XRD [6]. The

2D-XRD here unambiguously provides identification of crystalline phase and their powder character in all samples.

4 Magnetic measurements

The magnetic characterization of the two samples annealed at 400 and 500 °C was carried out using VSM. The measurements of M-H loops were carried out at room temperature, which is shown in Fig. 4a, b. The range of magnetic field (H)

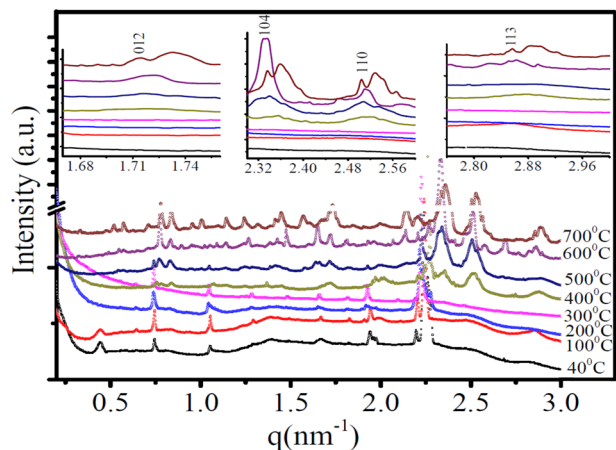
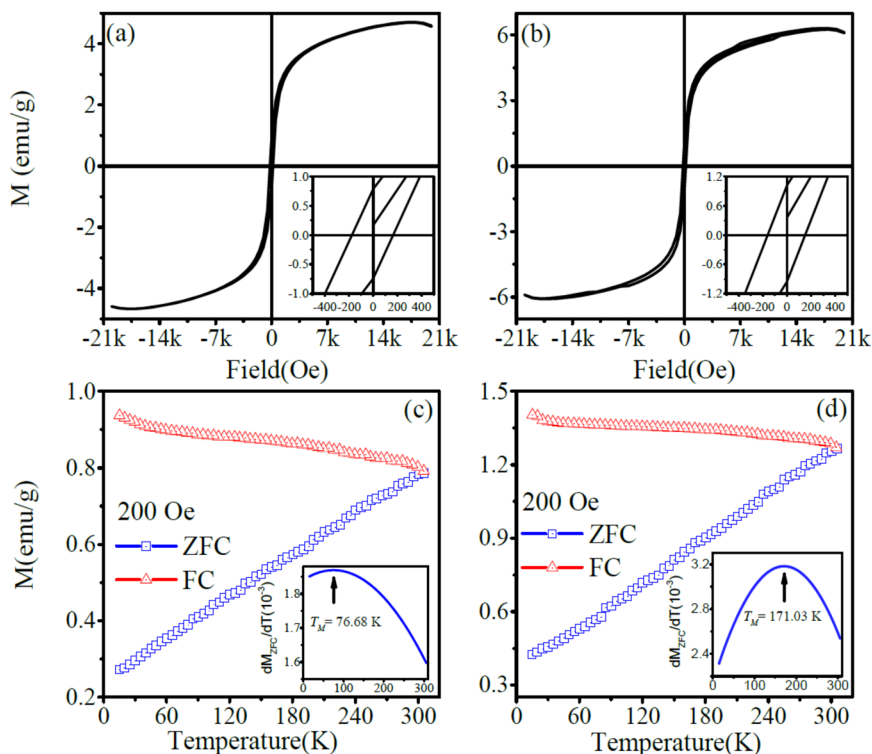


Fig. 3 Bottom: XRD peaks obtained after integrating 2D intensity arcs along polar angle (χ) from -90° to $+90^\circ$ for all samples annealed at different temperatures as shown in the graph. Top: Segmented portions of the XRD data showing the peaks with crystalline planes (012), (104), (110), (113) of α - Fe_2O_3 phase

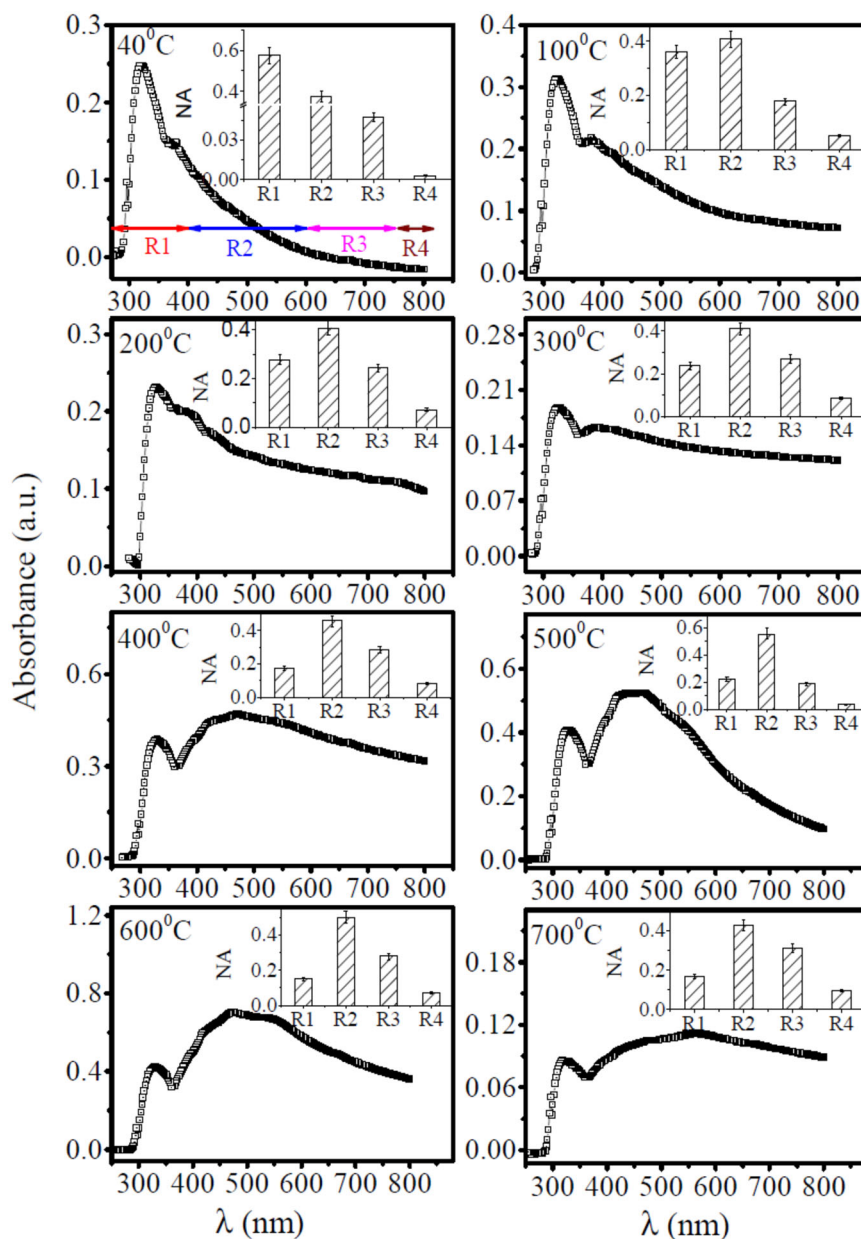
Fig. 4 Magnetization measurements using the VSM for the sample annealed at two different temperatures **a** 400 °C and **b** 500 °C respectively. Insets in top two panels provide zoomed portion of the same curve near origin; **c, d** Temperature dependence of M_{ZFC} and M_{FC} curves for the same samples as shown above in **a** and **b**. The insets in the lower panels, for the first derivative of a polynomial of third-order fitted with ZFC curve. The peak indicates the Morin temperature



was varied from -2 T to $+2\text{ T}$ in a cycle. A detailed study of magnetization at all annealing temperatures (40° – 700° C) was carried out earlier [6]. Among the various crystalline phases of Fe_2O_3 , maghemite (γ - Fe_2O_3) show the highest magnetic induction (74 – 103 emu/g), and the reported value of magnetic induction in hematite (α - Fe_2O_3) lies in the range from 1 – 15 emu/g [31–33]. The low value of magnetic induction in hematite is due to its anti-ferromagnetic properties, the magnetic induction in the anti-ferromagnetic systems arises mainly due to defects and disorder [32]. In this magnetic study, our objective was to study ZFC and FC at a constant magnetic field of 200 Oe . The samples had shown high magnetism in the annealing temperature range of 400 – 500° C . The magnetism in this range was partially attributed to the amorphous phase and partly due to the disordered structure at the surface of the nanoparticles leading to spin glass magnetic disorder [34]. The magnetization in units of emu/g was obtained by dividing the magnetic induction with the total sample mass. The deviations of magnetic moments with earlier study were likely due to the presence of unknown quantity of non-magnetic organic debris, which is external to magnetic system (Fe_2O_3). The magnetization values at different temperatures may suffer from different relative contributions of organic debris to the overall sample mass since the exact ratio of debris and magnetic component (Fe_2O_3) was not controlled.

The defects are responsible for demolishing the super-exchange interaction of the $\text{Fe}^{3+}\text{-O}^{2-}\text{-Fe}^{3+}$ leading to the ferromagnetic ordering [32, 35, 36]. A bulk phase of α -

Fig. 5 The absorption spectra of the samples using UV–VIS spectrometer. The powder samples were suspended in glycerol for the measurements at room temperature. The spectra are identified with the annealing temperature shown in each panel. The spectra are divided into four regions R1 (250–400 nm), R2 (400–600 nm), R3 (600–750 nm) and R4 (750–900 nm) for the identification of different processes. The inset in each panel shows the NA (normalized area) in each spectral region with a bar diagram

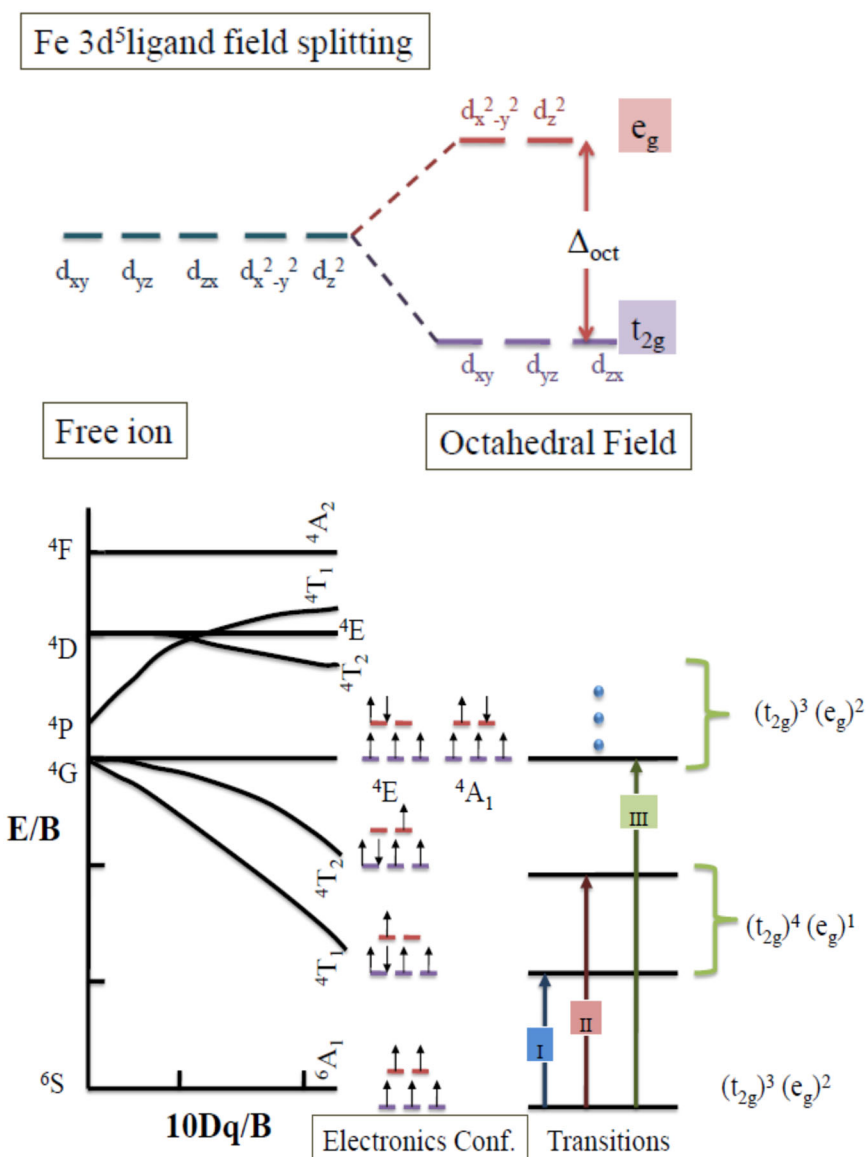


Fe_2O_3 shows weak magnetization (non-zero) between Morin temperature ($T_M \sim 263$ K) and Neel temperature ($T_N \sim 955$ K) due to spin canting [37]. The anti-ferromagnetic coupling of successive planes along (001) direction would mutually cancel out magnetic moments below Morin temperature. The Morin temperature was determined from the first derivative of the ZFC plot. The ZFC plot was first fitted with a polynomial of third-order and then the polynomial was differentiated to obtain first order derivative (dM_{ZFC}/dT) which is plotted in their corresponding insets in Fig. 4. The peak of the first derivative represents the Morin temperature [38]. It is well known that the Morin temperature depends on particle size and Morin temperature increases with particle size [39]. In our case, the Morin temperatures were found to

be ~ 77 K and ~ 171 K for annealing temperatures of 400°C and 500°C respectively. It can be inversely inferred from this observation that nanoparticle size is smaller at lower annealing temperature (400°C) as we could not directly estimate the particle size from XRD due to the absence of diffraction peak with regard to our earlier observations [6].

FC-ZFC curves bifurcate in two branches with successively increasing the gap up to 15 K. When cooled under the applied field (200 Oe), the magnetic induction increases with the decrease of cooling temperature. The thermal energy due to temperature is responsible for the randomization of spins. On cooling the thermal energy drops and the magnetic spins are more effectively aligned spins along the field that enhances the induction. In the absence of field

Fig. 6 Bottom: Tanabe-Sugano diagram for the Fe^{3+} in the octahedral coordination with the possible three optical transitions have different electronic configurations. Top: $\text{Fe } 3d^5$ ligand field splitting of degenerated five 3d orbitals into the level, t_{2g} and e_g in the octahedral field splitting (Δ_{oct}) [1, 46]



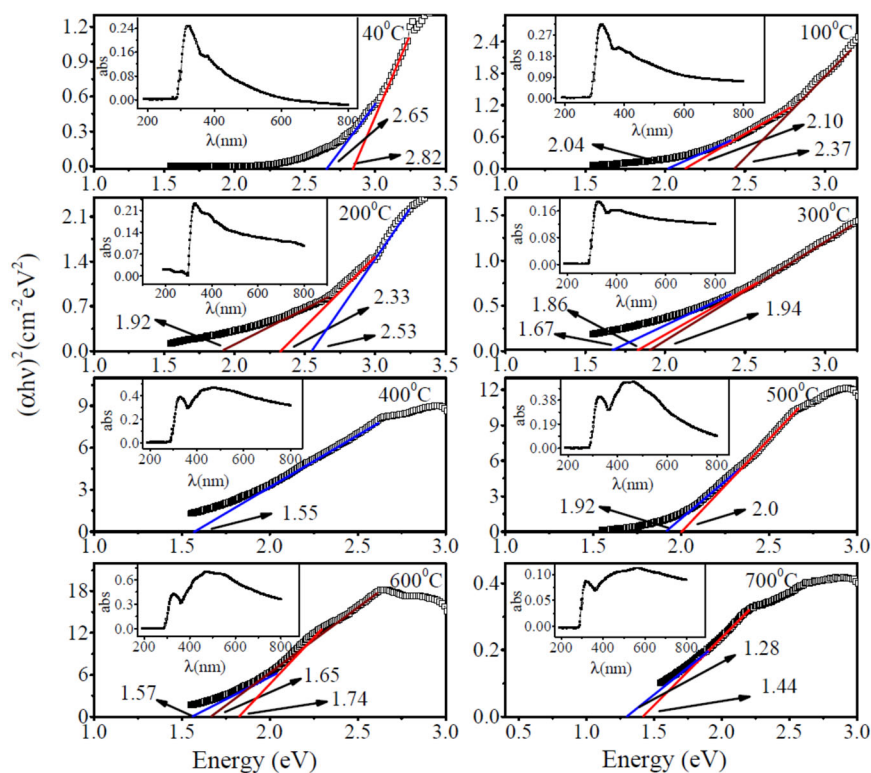
(ZFC), the magnetic induction decrease up to 15 K. In an anti-ferromagnetic system such as ($\alpha\text{-Fe}_2\text{O}_3$), the spin disorder causes a net magnetic moment even in absence of field. The spin disorder is caused by structural surface disorder and thermal randomization. By cooling, we reduce the effect of thermal randomization and hence net magnetic moment goes down with cooling. Magnetic coupling is often known to enhance ligand field (d-d) transition and pair excitations [39].

5 UV–VIS analysis

The optical absorption spectra in the range of 200–800 nm for all samples are shown in Fig. 5. The theory of optical absorption spectra for iron oxide compounds is well

established [1, 40]. The absorption spectra of Fe^{3+} ion complexes are optically active in the visible region. Therefore, these materials exhibit multiple color variations. The optical absorption occurs due to ligand-to-metal charge transfer (LMCT), ligand field transition (d-d transition) and pair excitation of neighboring Fe^{3+} ions due to magnetic coupling. Hematite ($\alpha\text{-Fe}_2\text{O}_3$) crystal forms a hexagonal structure where Fe^{3+} cation form octahedral coordination with O^{2-} anions. According to crystal field theory (CFT), 3d atomic orbitals of Fe are split into two sets of orbitals conventionally labeled as t_{2g} and e_g as shown in the Tanabe-Sugano diagram [1] in Fig. 6. The energy levels t_{2g} and e_g are further split by exchange energy which results in two sets of t_{2g} and e_g orbitals, one for majority spin and the other for minority spin. The ligand field transitions take place between states that arise from different electronic

Fig. 7 The Tauc's plots of all samples and samples are identified with the annealing temperature shown in each panel. The intersection of linear fits to the energy axis represents the band gap. The inset in each panel provides absorption spectra corresponding to each sample. All measurements were performed at room temperature 22 °C



configurations of the orbitals. LMCT, ligand field transitions and pair excitations had been identified from transient absorption decay using femtosecond time-resolved spectroscopy, since different processes are characterized with their unique decay-time [1]. LMCT, pair excitation and ligand field transition contribute to absorption in different spectral regions. For the identification of the processes, the entire wavelength range of the absorption spectra is divided into four regions [1, 41]: Region I (250–400 nm) mainly arises due to LMCT transitions and also from the Fe^{3+} ligand field transitions ${}^6\text{A}_1$ (${}^6\text{S}$) to ${}^4\text{T}_1$ (${}^4\text{P}$) at 290–310 nm, ${}^6\text{A}_1$ (${}^6\text{S}$) to ${}^4\text{E}$ (${}^4\text{D}$) and ${}^6\text{A}_1$ (${}^6\text{S}$) to ${}^4\text{T}_1$ (${}^4\text{D}$) at 360–380 nm. The spectroscopic symbols such as A, S, T, P, E and D have their conventional meaning as referred to earlier [42]. Region II (400–600 nm) is assigned to pair excitation processes ${}^6\text{A}_1$ (${}^6\text{S}$) + ${}^6\text{A}_1$ (${}^6\text{S}$) to ${}^4\text{T}_1$ (${}^4\text{G}$) + ${}^4\text{T}_1$ (${}^4\text{G}$) at 485–550 nm overlapping the ${}^6\text{A}_1$ (${}^6\text{S}$) to ${}^4\text{E}$, ${}^4\text{A}_1$ (${}^4\text{G}$) ligand field transition at 430 nm and the charge–transfer band. Region III (600–750 nm) is attributed due to ${}^6\text{A}_1$ (${}^6\text{S}$) to ${}^4\text{T}_2$ (${}^4\text{G}$) ligand field transition at around 640 nm. Region IV (750–900 nm) normally corresponds to transition ${}^6\text{A}_1$ (${}^6\text{S}$) to ${}^4\text{T}_1$ (${}^4\text{G}$) at around 900 nm. In our measurements, the scanning wavelength region extends to only 800 nm, thus region IV is partially included in the spectra shown in Fig. 5. The insets in Fig. 5 represent the normalized area (normalized integrated intensity) corresponding to these four regions in the form of column bars to highlight the contribution of the different processes. The normalized area

($\langle A \rangle$) defined in Eq. (1) as:

$$\langle A_i \rangle = \frac{A_i}{\sum_i A_i} \quad (1)$$

where A_i is area under the spectral regions ($i = 1$ for R_1 and so on). It is to be noted that there is no sharp distinction between these regions and the processes may overlap at the boundary of these defined regions, yet such demarcation provides the convenience of analysis of absorption spectra.

For the “as prepared” sample (40 °C), the absorption mainly occurs in region I, which suggests the dominance of LMCT processes. As the annealing temperature of the samples increases, the absorption process shifts toward the red end of the spectrum. For the sample sintered at 500 °C, the absorption in region II is highly dominant which is caused by pair excitation neighboring Fe^{3+} ions that often results due to magnetic coupling. The study of magnetic measurements also shows a stronger magnetic moment (Fig. 4) in this temperature range (400–500 °C). The sample annealed at 700 °C marks the further red shift toward region III which arises due to ligand field transition ${}^6\text{A}_1$ (${}^6\text{S}$)– ${}^4\text{T}_2$ (${}^4\text{G}$). Rather the absorption spectrum becomes almost flat in the entire visible region which signifies that all three processes are contributing evenly with the pair transition process having slight dominance over LMCT and ligand field (d-d) transitions. The activation of different processes in separate wavelength ranges leads to the shifting of the band edge. The absorption band edge was determined using the

Table 2 Optical band gap energy with the error calculated from Tauc's plots for α -Fe₂O₃ in samples annealed at different temperature

Annealing temperature (°C)	Optical band gap (eV)		
	Linear slope 1	Linear slope 2	Linear slope 3
40	2.65 ± 0.01	2.82 ± 0.01	–
100	2.04 ± 0.004	2.10 ± 0.01	2.37 ± 0.01
200	1.92 ± 0.003	2.33 ± 0.01	2.53 ± 0.02
300	1.67 ± 0.015	1.86 ± 0.007	1.94 ± 0.04
400	1.55 ± 0.003	–	–
500	1.92 ± 0.002	2.0 ± 0.006	–
600	1.57 ± 0.004	1.65 ± 0.006	1.74 ± 0.003
700	1.28 ± 0.005	1.44 ± 0.004	–

Tauc's relation [43] as the following Eq. (2):

$$\alpha h\nu = A(h\nu - E_g)^n \quad (2)$$

Here, n is an exponent that is 1/2 for direct band gap and 2 for indirect band gap [9, 44]. The above equation fits well for $n = 1/2$ suggesting a direct band gap system. We plotted $(\alpha h\nu)^2$ vs. $h\nu$ for all samples that are shown in Fig. 7 with insets representing the whole absorption spectra. The linear extrapolation that intersects the energy axis represents the value of the bandgap. It can be observed that often 2 or 3 linear slopes existed for the various samples. These different band edges correspond to different transition processes involved in the absorption. The presence of various processes also results in the blurring of the absorption edge. The different band edges found using the above process are arranged in Table 2 for convenience. The shifting of the band edge from 2.65 to 1.28 eV is a very large red shift that marks a kind of insulator-to-semiconductor transition.

6 Discussion

The optical properties of iron-based TMO arise from heterogeneity of electronic states due to the multiplicity of coordination of Fe³⁺ ion with neighboring ligands. We have a set of samples that include, at one end, dry ferritin powder (40 °C) and hematite crystalline phase (700 °C) at the other end. The samples in the intermediate temperature range provide a set of iron oxide with a varying degree of crystalline order between these two ends. The core of a native Ferritin constitutes ferrihydrite (FeOOH) molecules that could move in and out of the cavity for carrying out biological processes [14]. A dry ferritin powder would contain densely packed molecules that are very different from continuous solid phase such as α -Fe₂O₃. The annealing at higher temperatures gives way to the

formation of Fe₂O₃ after releasing of water from the ferrihydrite molecules [6, 14]. The Fe₂O₃ initially in the solid phase begins to crystallize at around 500 °C, which then transforms into a stable structure of hematite at 700 °C. The organic shell of the Ferritin begins to erode at around 300 °C and it is almost destroyed around 450 °C which is evident from the EDX analysis in Fig. 1. The crystalline phase of α -Fe₂O₃ begins to appear beyond 400 °C which indicates that the crystallization of Fe₂O₃ is related to the destruction of the organic shell of ferritin. It is obvious that the breaking of the shell allows the particles to grow through sintering and coalescence processes. The particles grow bigger in the form of needles or flakes as seen in the SEM images. It can be seen that the optical absorption strongly depends on the temperature of the thermal treatment. For dry ferritin powder (40°), the optical absorption mainly takes place in the UV limit which represents high energy LMCT transitions. Pair transitions and ligand field (d-d) transitions are mostly absent. This observation is consistent with the fact that iron molecular complexes do not constitute a continuous solid justifying the absence of pair excitations and coordinated ligand field transitions. As the sintering temperature is increased the spectrum tail shifts toward the red end. At 400–500 °C, the intensity of pair-transitions eclipses the LMCT transitions. In this temperature range, the samples show relatively strong magnetic intensity. The pair transitions are associated with the magnetic coupling of neighboring Fe³⁺ ions through O²⁻ ions. In this intermediate temperature range, the crystalline phase begins to emerge with the amorphous surface disorder which is responsible for stronger magnetism since the exact cancellation of magnetic moments originating from anti-parallel spins was not possible due to the presence of surface disorder. In this temperature range, iron oxide forms a solid phase but the proper crystalline order is lacking. In the high-temperature range (500–700 °C), as the crystalline phase of α -Fe₂O₃ becomes more distinct, the spectrum was further red shifted due to activation of ligand field transition from ⁶A₁ (⁶S) to ⁴T₂ (⁴G). In principle, all such electronic transitions are Laporte and spin forbidden. But transitions become allowed in practice due to magnetic coupling of neighboring Fe³⁺ ions and hybridization of Fe 3d orbitals with O 2p orbitals [1]. The α -Fe₂O₃ forms the corundum structure with octahedral coordination of Fe³⁺ ions with neighboring O²⁻ ions. The multiplicity of the electronic state arises due to high spin and low spin configurations. The ligand field transition (d-d) is described by CFT with the help of the Tanabe-Sugano diagram [1]. The optical spectrum of the sample with the highest temperature (700 °C) treatment spreads almost uniformly through the UV and visible range with a slight bulge of intensity in the middle of the visible region due to magnetically coupled pair transitions. It means all processes such as LMCT, pair excitation and d-d transitions are active for the samples at the high end of annealing temperature. In the

continuous solid phase, d-d electronic levels are rather d-d bands. The width of the bands depends on the degree of overlapping of atomic orbitals. The distribution of nanoparticle size, which is a very common feature, will result in a varying degree of overlapping and hence a varied range of bandwidths. The distribution of particle size would thus result in the blurring of the absorption band edge. Tauc's relation was used to find the type of the band gap (direct or indirect) and also to estimate the absorption band edge. The fittings of the absorption spectra suggest a direct band gap transition. Both kinds of results are available for direct as well as indirect band gaps for the α -Fe₂O₃ system in the published literature [44, 45]. Though the absorption edge with minimum energy (or maximum wavelength) is the true band edge but multiplicity of linear slopes occurs as other stronger absorption due to pair excitation and LMCT dominates at the high energy end of the spectrum. The shifting of the minimum energy band edge from 2.65 to 1.28 eV is remarkable which indeed highlights the scope of tailoring of band gap of the material transforming an insulator into a semiconductor.

7 Conclusions

An aqueous sol of Ferritin was dried and heat treated to synthesize materials with tuneable optical properties. The samples were synthesized using the sol-gel method and varied thermal treatment was given to bring about the phase change from ferrihydrite to hematite crystalline phase (α -Fe₂O₃). The optical absorption was studied in a viscous liquid medium by UV-visible spectroscopy. 2D-XRD analysis confirms the presence of hematite crystalline phase and that the crystallites are in powder form in all samples. EDX analysis found that the thermal treatment burns down the organic shell of Ferritin at around 450 °C. It was noted that the crystallization of Fe₂O₃ took place after the destruction of the organic shell. The optical spectra of the samples have strong bearing of annealing temperature, which in turn implies that variation in phases of the Fe³⁺ ionic compound enriches the optical spectrum through activation of pair excitation and ligand field transitions to add to LMCT processes. In the mid temperature range of 400–500 °C, the pair excitation mechanism become strong and dominates over LMCT. The mid temperature range was also characterized with strong magnetic induction, reaffirming that the pair excitations are usually a result of magnetic coupling of Fe³⁺ ion pairs in the system. In the high-temperature range of 500–700 °C, ligand field (d-d) transitions become active to shift the absorption edge toward the red end. This study brings about a facile way of tuning the band gap from 2.65 to 1.28 eV, which covers a wide range for optical and electronic applications.

Acknowledgements SK thankfully acknowledges the University Grants Commission for National Fellowship scheme for SC (erstwhile-RGNF, Lett. No. F1-17.1/2016-17/RGNF-2015-17-SC-HIM-18502/(SA-III/Website)) for the financial support as fellowship toward pursuance of Ph.D. We acknowledge the UV-VIS facility established at the Himachal Pradesh University, Shimla. We also acknowledge the AMRC, IIT Mandi for SEM facility (JFEI, Nova Nano SEM-450).

Compliance with ethical standards

Conflict of interest The authors declare no competing interests.

References

1. He YP, Miao YM, Li CR et al. (2005) Size and structure effect on optical transitions of iron oxide nanocrystals. *Phys Rev B - Condens Matter Mater Phys* 71:1–9. <https://doi.org/10.1103/PhysRevB.71.125411>
2. MacHala L, Tuček J, Zbořil R (2011) Polymorphous transformations of nanometric iron(III) oxide: a review. *Chem Mater* 23:3255–3272. <https://doi.org/10.1021/cm200397g>
3. Ivantsov R, Ivanova O, Zharkov SM et al. (2020) Magnetic circular dichroism in the canted antiferromagnet α -Fe₂O₃: bulk single crystal and nanocrystals. *J Magn Magn Mater* 498:166208. <https://doi.org/10.1016/j.jmmm.2019.166208>
4. Bhowmik RN, Sarvanan A (2010) Surface magnetism, Morin transition, and magnetic dynamics in antiferromagnetic α -Fe₂O₃ (hematite) nanograins. *J Appl Phys* 107:053916–1–10
5. Frandsen C, Mørup S (2005) Spin rotation in α -Fe₂O₃ nanoparticles by interparticle interactions. *Phys Rev Lett* 94(1–4):027202
6. Kumar S, Thakur A, Gupta SK et al. (2020) A facile route to synthesis of ferromagnetic and antiferromagnetic phases of iron oxide nanoparticles by controlled heat treatment of ferritin. *J Supercond Nov Magn* 33:3841–3852. <https://doi.org/10.1007/s10948-020-05649-1>
7. Sharma P, Dhiman S, Kumari S, et al. (2019) Revisiting the physiochemical properties of Hematite (α -Fe₂O₃) nanoparticle and exploring its bio-environmental application. *Mater Res Express* 6. <https://doi.org/10.1088/2053-1591/ab30ef>
8. Sivula K, Zboril R, Le Formal F et al. (2010) Photoelectrochemical water splitting with mesoporous hematite prepared by a solution-based colloidal approach. *J Am Chem Soc* 132:7436–7444. <https://doi.org/10.1021/ja101564f>
9. Kumar P, Rawat N, Hang DR et al. (2015) Controlling band gap and refractive index in dopant-free α -Fe₂O₃ films. *Electron Mater Lett* 11:13–23. <https://doi.org/10.1007/s13391-014-4002-0>
10. Uchida M, Flenniken ML, Allen M et al. (2006) Targeting of cancer cells with ferrimagnetic ferritin cage nanoparticles. *J Am Chem Soc* 128:16626–16633. <https://doi.org/10.1021/ja0655690>
11. Bhowmik RN, Mitra P, Choudhury RJ, Reddy VR (2020) Substrate effect on the structural phase formation and magnetic properties of α -Fe₂O₃ and Ti doped α -Fe₂O₃ thin films. *Appl Surf Sci* 501:144224. <https://doi.org/10.1016/j.apsusc.2019.144224>
12. Lu Y, Yin Y, Mayers BT, Xia Y (2002) Modifying the surface properties of superparamagnetic iron oxide nanoparticles through a sol-gel approach. *Nano Lett* 2:183–186. <https://doi.org/10.1021/nl015681q>
13. Gupta AK, Gupta M (2005) Synthesis and surface engineering of iron oxide nanoparticles for biomedical applications. *Biomaterials* 26:3995–4021. <https://doi.org/10.1016/j.biomaterials.2004.10.012>

14. Jutz G, Van Rijn P, Santos Miranda B, Böker A (2015) Ferritin: a versatile building block for bionanotechnology. *Chem Rev* 115:1653–1701. <https://doi.org/10.1021/cr400011b>
15. Volatron J, Carn F, Kolosnjaj-Tabi J et al. (2017) Ferritin protein regulates the degradation of iron oxide nanoparticles. *Small* 13:1–13. <https://doi.org/10.1002/sml.201602030>
16. He D, Marles-Wright J (2015) Ferritin family proteins and their use in bionanotechnology. *N Biotechnol* 32:651–657. <https://doi.org/10.1016/j.nbt.2014.12.006>
17. Choi WJ, Yano K, Cha M, et al. (2022) Chiral phonons in microcrystals and nanofibrils of biomolecules. *Nat Photon*. <https://doi.org/10.1038/s41566-022-00969-1>
18. Xing X, Chen M, Gong Y et al. (2020) Building memory devices from biocomposite electronic materials. *Sci Technol Adv Mater* 21:100–121. <https://doi.org/10.1080/14686996.2020.1725395>
19. Lv Z, Zhou Y, Han ST, Roy VAL (2018) From biomaterial-based data storage to bio-inspired artificial synapse. *Mater Today* 21:537–552. <https://doi.org/10.1016/j.mattod.2017.12.001>
20. Cobo I, Li M, Sumerlin BS, Perrier S (2015) Smart hybrid materials by conjugation of responsive polymers to biomacromolecules. *Nat Mater* 14:143–149. <https://doi.org/10.1038/nmat4106>
21. Raeis-Hosseini N, Lee JS (2017) Resistive switching memory using biomaterials. *J Electroceram* 39:223–238. <https://doi.org/10.1007/s10832-017-0104-z>
22. Singh A, Konovalov O, Novak J, Vorobiev A (2010) The sequential growth mechanism of a protein monolayer at the air-water interface. *Soft Matter* 6:3826–3831. <https://doi.org/10.1039/b925365c>
23. Singh A, Konovalov O (2013) Measuring elastic properties of a protein monolayer at water surface by lateral compression. *Soft Matter* 9:2845–2851. <https://doi.org/10.1039/c2sm26410b>
24. Hench LL, West JK (1990) The sol-gel process. *Chem Rev* 90:33–72. <https://doi.org/10.1021/cr00099a003>
25. Alagiri M, Hamid SBA (2015) Sol-gel synthesis of α -Fe₂O₃ nanoparticles and its photocatalytic application. *J Sol-Gel Sci Technol* 74:783–789
26. Aydin C, Mansour SA, Alahmed ZA, Yakuphanoglu F (2012) Structural and optical characterization of sol-gel derived boron doped Fe₂O₃ nanostructured films. *J Sol-Gel Sci Technol* 62:397–403. <https://doi.org/10.1007/s10971-012-2740-8>
27. Mohanty A, Parida A, Raut RK, Behera RK (2022) Ferritin: a promising nanoreactor and nanocarrier for bionanotechnology. *ACS Bio Med Chem Au*. <https://doi.org/10.1021/acsbiochemau.2c00003>
28. Xia C, Jia Y, Tao M, Zhang Q (2013) Tuning the band gap of hematite α -Fe₂O₃ by sulfur doping. *Phys Lett Sect A: Gen At Solid State Phys* 377:1943–1947
29. MacHala L, Zboril R, Gedanken A (2007) Amorphous iron (III) oxide—a review. *J Phys Chem B* 111:4003–4018. <https://doi.org/10.1021/jp064992s>
30. Kim CY (2020) Atomic structure of hematite (α -Fe₂O₃) nanocube surface; synchrotron X-ray diffraction study. *Nano-Struct Nano-Objects* 23:100497. <https://doi.org/10.1016/j.nanoso.2020.100497>
31. Cao D, Li H, Pan L et al. (2016) High saturation magnetization of γ 3-Fe₂O₃ nano-particles by a facile one-step synthesis approach. *Sci Rep* 6:1–9. <https://doi.org/10.1038/srep32360>
32. Wu J, Mao S, Ye ZG et al. (2010) Room-temperature weak ferromagnetism induced by point defects in α -Fe₂O₃. *ACS Appl Mater Interfaces* 2:1561–1564. <https://doi.org/10.1021/am1002052>
33. Bhavani P, Rajababu CH, Arif MD et al. (2017) Synthesis of high saturation magnetic iron oxide nanomaterials via low temperature hydrothermal method. *J Magn Magn Mater* 426:459–466. <https://doi.org/10.1016/j.jmmm.2016.09.049>
34. Kodama RH, Berkowitz AE, McNiff EJJ, Foner S (1996) Surface spin disorder in NiFe₂O₄ nanoparticles. *Phys Rev Lett* 77:394–397
35. Phu ND, Ngo DT, Hoang LH, et al. (2011) Crystallization process and magnetic properties of amorphous iron oxide nanoparticles. *J Phys D Appl Phys* 44. <https://doi.org/10.1088/0022-3727/44/34/345002>
36. Silva MF, De Oliveira LAS, Ciciliati MA, et al. (2013) Nanometric particle size and phase controlled synthesis and characterization of γ -Fe₂O₃ or (α + γ)-Fe₂O₃ by a modified sol-gel method. *J Appl Phys* 114. <https://doi.org/10.1063/1.4821253>
37. Bhowmik RN, Saravanan A (2010) Surface magnetism, Morin transition, and magnetic dynamics in antiferromagnetic α -Fe₂O₃ (hematite) nanograins. *J Appl Phys* 107. <https://doi.org/10.1063/1.3327433>
38. Chakrabarty S, Jana TK, De K, et al. (2014) Morphology dependent magnetic properties of α -Fe₂O₃ nanostructures. *Mater Res Express* 1. <https://doi.org/10.1088/2053-1591/1/4/046104>
39. Biju CS, Raja DH, Padiyan DP (2014) Glycine assisted hydrothermal synthesis of α -Fe₂O₃ nanoparticles and its size dependent properties. *Chem Phys Lett* 610–611:103–107. <https://doi.org/10.1016/j.cplett.2014.07.024>
40. Sherman DM, Waite TD (1985) Electronic spectra of Fe³⁺ oxides and oxide hydroxides in the near IR to near UV. *Am Mineralogist* 70:1262–1269
41. Wheeler DA, Wang G, Ling Y et al. (2012) Nanostructured hematite: synthesis, characterization, charge carrier dynamics, and photoelectrochemical properties. *Energy Environ Sci* 5:6682–6702. <https://doi.org/10.1039/c2ee00001f>
42. Huheey JE, Keiter EA, Keiter RL (2000) Inorganic chemistry: principles of structure and reactivity, 4th edn. Pearson Education Asia Pte. Ltd., New York
43. Tauc J, Grigorovici R, Vancu A (1966) Optical properties and electronic structure of amorphous germanium. *Phys Status Solidi* 15:627–637. https://doi.org/10.1007/978-1-4757-1123-3_5
44. Mallick P, Dash BN (2013) X-ray diffraction and UV-visible characterizations of α -Fe₂O₃ nanoparticles annealed at different temperature. *Nanosci Nanotechnol* 3:130–134. <https://doi.org/10.5923/j.nn.20130305.04>
45. Seo O, Tayal A, Kim J et al. (2019) Tuning of structural, optical band gap, and electrical properties of room-temperature-grown epitaxial thin films through the Fe₂O₃:NiO ratio. *Sci Rep* 9:1–9. <https://doi.org/10.1038/s41598-019-41049-9>
46. Choi S, Lefèvre C, Roulland F et al. (2012) Optical transitions in magnetoelectric Ga_{0.6}Fe_{1.4}O₃ from 0.73 to 6.45 eV. *J Vac Sci Technol B* 30:41204. <https://doi.org/10.1116/1.4721649>

Publisher's note Springer Nature remains neutral with regard to jurisdictional claims in published maps and institutional affiliations.

Springer Nature or its licensor (e.g. a society or other partner) holds exclusive rights to this article under a publishing agreement with the author(s) or other rightsholder(s); author self-archiving of the accepted manuscript version of this article is solely governed by the terms of such publishing agreement and applicable law.